UC Berkeley
UC Berkeley Previously Published Works

Title
Zn-Ion Transporting, In Situ Formed Robust Solid Electrolyte Interphase for Stable Zinc Metal Anodes over a Wide Temperature Range

Permalink
https://escholarship.org/uc/item/8mz8n8vf

Journal
ACS Energy Letters, 8(3)

ISSN
2380-8195

Authors
Xiong, Peixun
Kang, Yingbo
Yao, Nan
et al.

Publication Date
2023-03-10

DOI
10.1021/acsenergylett.3c00154

Peer reviewed

eScholarship.org Powered by the California Digital Library
University of California

ACS Energy LETTERS

http://pubs.acs.org/journal/aelccp

Zn-Ion Transporting, *In Situ* Formed Robust Solid Electrolyte Interphase for Stable Zinc Metal Anodes over a Wide Temperature Range

Peixun Xiong, Yingbo Kang, Nan Yao, Xiang Chen, Haiyan Mao, Woo-Sung Jang, David M. Halat, Zhong-Heng Fu, Min-Hyoung Jung, Hu Young Jeong, Young-Min Kim, Jeffrey A. Reimer, Qiang Zhang, and Ho Seok Park*

Cite This: *ACS Energy Lett.* 2023, 8, 1613−1625

Read Online

ACCESS | Metrics & More | Article Recommendations | Supporting Information

ABSTRACT: **Hydrogen evolution, corrosion, and dendrite formation in the Zn anodes limit their practical applications in aqueous Zn metal batteries. Herein, we propose an interfacial chemistry regulation strategy that uses hybrid electrolytes of water and a polar aprotic *N*,*N*-dimethylformamide to modify the Zn^{2+}-solvation structure and *in situ* form a robust and Zn^{2+}-conducting $Zn_5(CO_3)_2(OH)_6$ solid electrolyte interphase (SEI) on the Zn surface to achieve stable and dendrite-free Zn plating/stripping over a wide temperature range. As confirmed by ^{67}Zn nuclear magnetic resonance relaxometry, electrochemical characterizations, and molecular dynamics simulation, the electrochemically and thermally stable $Zn_5(OH)_6(CO_3)_2$-contained SEI achieved a high ionic conductivity of 0.04 to 1.27 mS cm^{-1} from −30 to 70 °C and a thermally activated fast Zn^{2+} migration through the [010] plane. Consequently, extremely stable Zn-ion hybrid capacitors in hybrid electrolytes are demonstrated with high capacity retentions and Coulombic efficiencies over 14,000, 10,000, and 600 cycles at 25, −20, and 70 °C, respectively.**

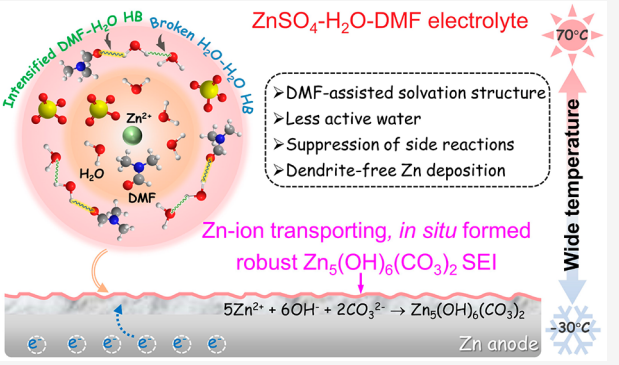

Rechargeable aqueous zinc metal batteries (AZMBs) have gained considerable attention as a replacement for conventional lithium-ion batteries (LIBs) because of the essential advantages of zinc (Zn) metal anodes, which includes high theoretical gravimetric and volumetric capacities (820 mA h g^{-1} and 5855 mA h cm^{-3}, respectively), low cost, and natural abundance.[1−4] Given by the appropriate plating/stripping potential of Zn metals, AZMBs further benefit from the advantage of their high ionic conductivity and environmental benignity when operated in aqueous electrolytes. Although this enhances the electrochemistry between Zn metal and aqueous electrolyte, the electrochemical performance and stability of AZMBs deteriorate owing to Zn dendrite formation, corrosion, and hydrogen evolution reaction (HER).[5−9] These unfavorable reactions are more critical at higher temperatures (>60 °C), as they can be accelerated by thermal activation, thereby seriously degrading the stability of the batteries.[10] Furthermore, the volatilization of water can reduce the ionic conductivity of the electrolyte. Conversely, the reversible deposition/stripping of Zn is more sluggish even at lower temperatures (<0 °C) owing to freezing, increased viscosity, and salt precipitation.[11] These dilemmas limit the high efficiency and long-term stability of AZMBs operating in a wide temperature range of "both below 0 °C and above 60 °C."

Herein, we report the Zn^{2+}-ion conductive and robust solid electrolyte interphase (SEI) *in situ* formed by the hybrid-electrolyte-regulating solvation structure and interfacial chemistry for highly efficient and extremely stable AZMBs at low (−30 °C) and high (70 °C) temperatures for the first time. Hybrid electrolytes containing water and other soluble substances (solid or organic liquid) have been recently

Received: January 19, 2023
Accepted: February 21, 2023
Published: February 27, 2023

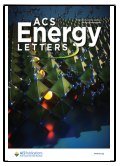

Downloaded via UNIV OF CALIFORNIA BERKELEY on June 20, 2024 at 21:33:52 (UTC).
See https://pubs.acs.org/sharingguidelines for options on how to legitimately share published articles.

ACS Publications © 2023 American Chemical Society

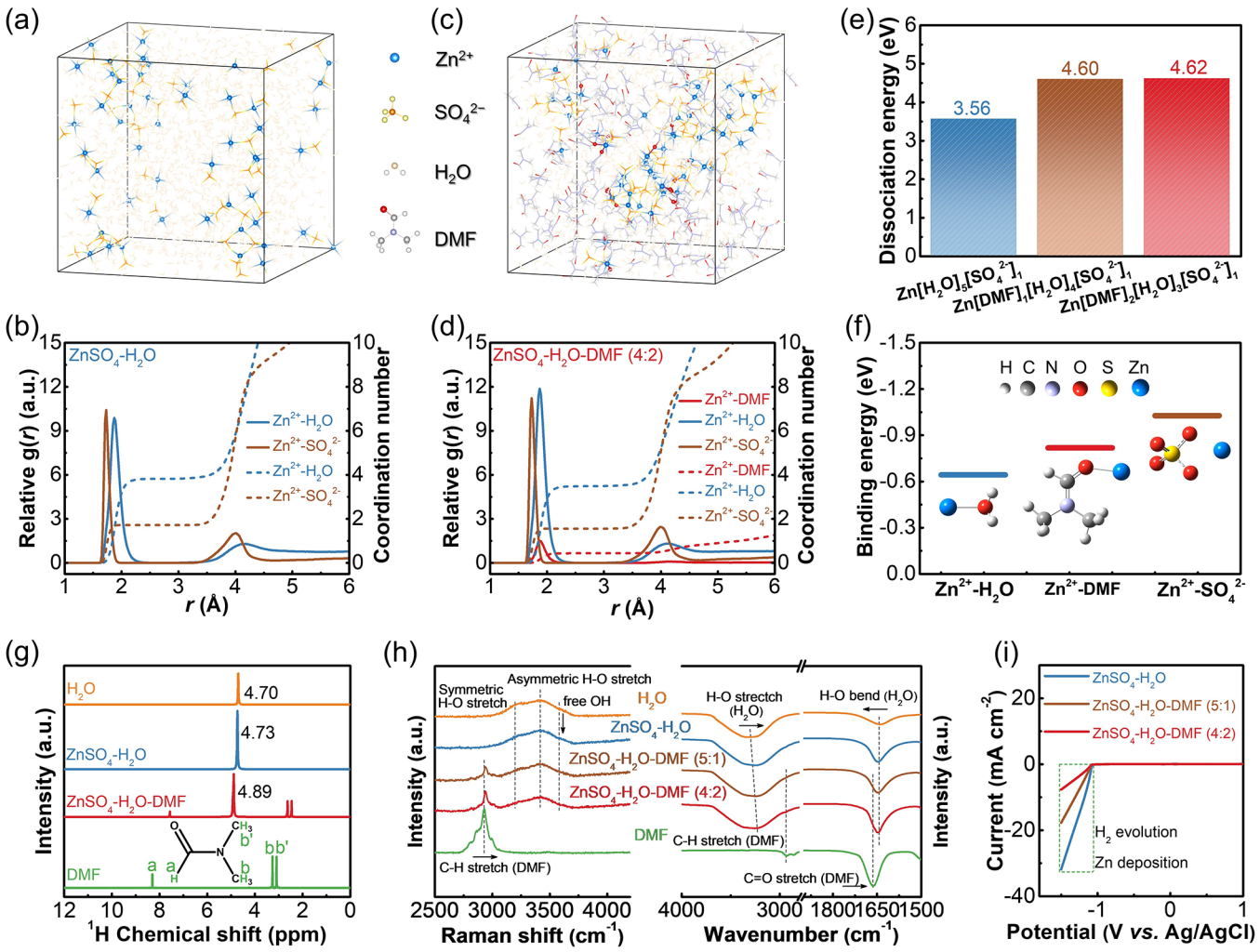

Figure 1. Solvation structure analysis of hybrid electrolytes. Snapshots of (a) $ZnSO_4$−H_2O and (c) $ZnSO_4$−H_2O−DMF electrolytes during MD simulations. Radial distribution functions (RDFs) and coordination number distribution functions obtained from MD simulations for (b) $ZnSO_4$−H_2O and (d) $ZnSO_4$−H_2O−DMF electrolytes. (e) Dissociation energy of different $Zn^{2+}[DMF]_x[H_2O]_y[SO_4^{2-}]_z$ complexes. (f) Relative binding energy for Zn^{2+} with different species obtained from DFT calculations. (g) ^1H NMR spectra of $ZnSO_4$−H_2O and $ZnSO_4$−H_2O−DMF electrolytes. (h) Raman (left) and FTIR (right) spectra of H_2O, DMF, and different electrolytes. (i) LSV response curves of different electrolytes at 0.5 mV s^{-1}.

developed to modify the local- and/or bulk-solvated environment of water to improve the thermodynamic stability.[12−16] Examples of hybrid electrolytes include triethyl phosphate,[16] diethyl ether,[17] ethylene glycol,[18] dimethyl sulfoxide,[19] and acetonitrile,[20] which could enhance the reversibility of Zn deposition for long-term cyclability up to 2000 h. However, these hybrid electrolytes are limited by narrow operating temperatures and/or rates (1 mA cm^{-2} and 1 mA h cm^{-2}). In particular, a fundamental understanding about Zn^{2+}-ion transport mechanism of SEI layer, which is *in situ* formed by hybrid electrolytes, at wide temperatures has yet to be explored.

To overcome these impediments, the proposed chemical strategy provides a simple and effective method for formulating hybrid electrolytes with a polar aprotic solvent, including a higher Gutmann donor number than that of water and *in situ* SEI-forming capability (Figure S1). First, the polar aprotic solvent was selected to disrupt the hydrogen bonding networks coordinating with Zn^{2+}, partially substitute the coordinating H_2O, and subsequently modify the solvated structure. This modified solvated structure is assumed to increase the Zn^{2+} desolvation energy, thereby regulating the kinetics for homogeneous Zn deposition while insignificantly slowing the Zn^{2+} transport.[16−20] Moreover, for the low-temperature operation of AZMBs, the Zn^{2+} transport of the solvated structure was constant even at −30 °C which the freezing of H_2O is inhibited. Notably, this solvent can be decomposed at the interface to *in situ* fabricate a rapid Zn^{2+} transporting and robust SEI on Zn anodes. This newly *in situ* formed $Zn_5(CO_3)_2(OH)_6$ SEI achieves high Zn^{2+}-ion conductivity over a wide temperature range, even and is so electrochemically, mechanically, and thermally stable that the dendrite formation can be suppressed at extreme conditions at 70 °C. To prove our hypothesis, we selected polar aprotic *N*,*N*-dimethylformamide (DMF), donor number of 26.6 larger than 18 of H_2O[21] and freezing and boiling points of −61 and 153 °C,[22] that can satisfy all the above requirements. Therefore, as schematically illustrated in Figure S1, the $ZnSO_4$−H_2O−DMF hybrid electrolyte allows uniform and dense Zn deposition on the Zn anode for significantly enhanced performance, while preventing the HER, corrosion, and dendrite formation, which

https://doi.org/10.1021/acsenergylett.3c00154
ACS Energy Lett. 2023, 8, 1613−1625

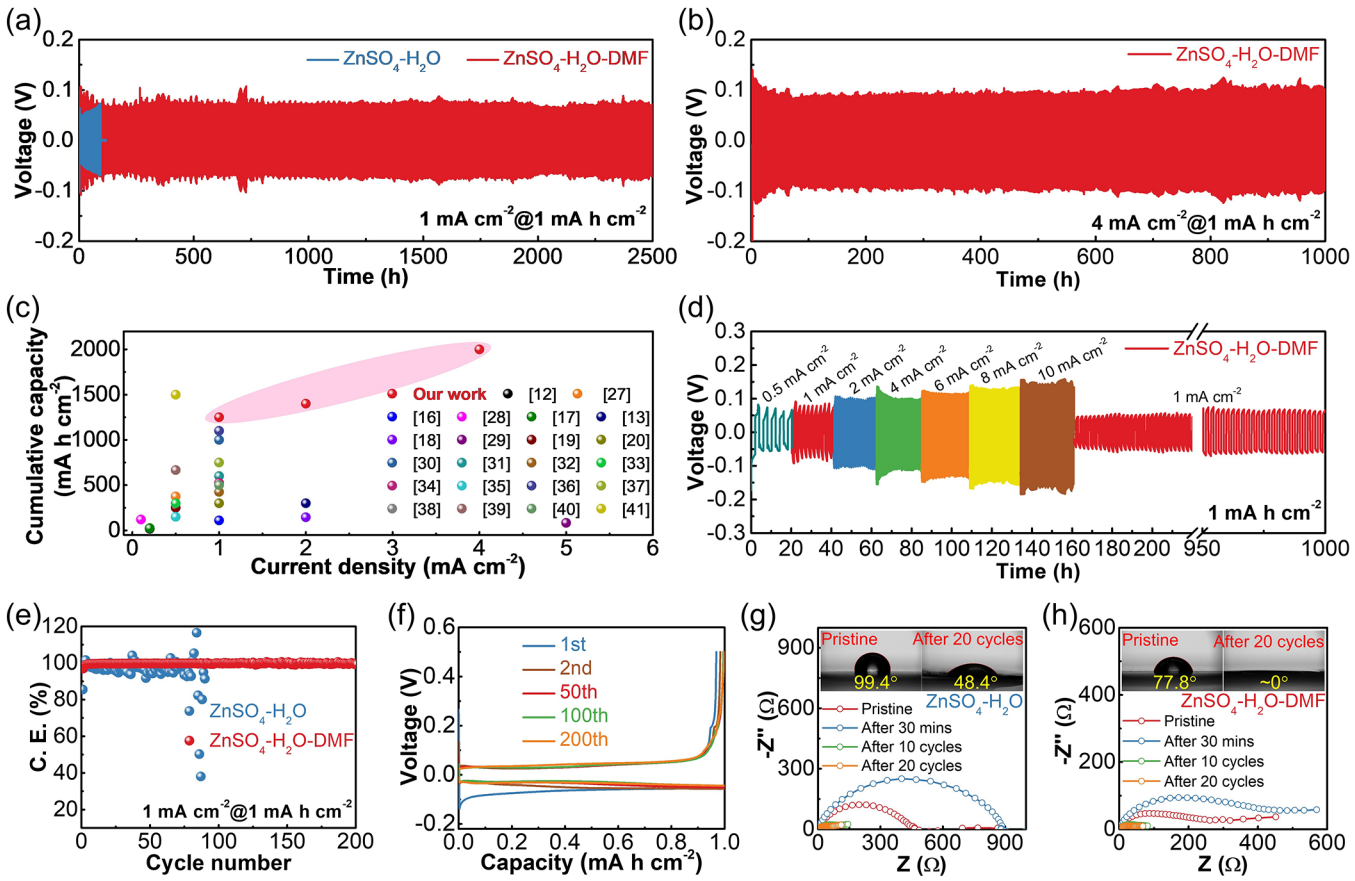

Figure 2. Electrochemical performances of Zn anodes in various electrolytes. Cycling performance of Zn||Zn symmetric cells in different electrolytes at (a) 1 mA cm^{-2} and (b) 4 mA cm^{-2} for 1 mA h cm^{-2}. The voltage increase in (a) at around 700 h is caused by the temperature drop due to power failure of the temperature-controlled equipment. (c) Comparison of the cumulative capacity with recently reported Zn anodes using optimization strategies. (d) Rate performance of Zn||Zn symmetric cell in $ZnSO_4$−H_2O−DMF at various current densities. (e) CE of Zn plating/stripping on Cu foil in different electrolytes and (f) the corresponding charge−discharge profiles in the $ZnSO_4$−H_2O−DMF electrolyte at 1 mA cm^{-2} for 1 mA h cm^{-2}. Nyquist plots of Zn||Zn symmetric cells in (g) $ZnSO_4$−H_2O and (h) $ZnSO_4$−H_2O−DMF before cycle, rest 30 min, and after cycling (insertion are the contact angles before and after 20 cycles).

is attributed to the synergistic effect of modified solvation structure and fast Zn^{2+} conducting $Zn_5(OH)_6(CO_3)_2$.

Solvation Structure Analysis of Hybrid Electrolyte. It has been known that the free water molecules can combine with Zn^{2+} ions and solvate to form a hydrated Zn ion of $[Zn(H_2O)_6]^{2+}$ in the most common $ZnSO_4$ electrolytes.[12,23] In this study, a series of 2 M $ZnSO_4$−H_2O−DMF hybrid electrolytes with various H_2O to DMF volume ratios (6:0, 5:1, 4:2, 3:3, 2:4, 1:5, and 0:6) were prepared (Figure S2). Homogenous solutions were formed when the H_2O/DMF ratios were 5:1 and 4:2. However, apparent recrystallization of $ZnSO_4$ occurred when the H_2O to DMF ratio increased up to 3:3, indicating that the involvement of DMF in modifying the solvation structure of Zn^{2+}, which could be damaged by excess DMF (Figures S1 and S2).[24] Although DMF is dissolved in H_2O in any proportions to construct a hydrogen bonding (HB), its solubility to $ZnSO_4$ is not sufficiently high due to the antisolvent effect against an aqueous $ZnSO_4$ electrolyte.[25,26] Accordingly, the H_2O to DMF ratio was controlled in the range from 6:0 to 2:4.

The solvation structure of the hybrid electrolytes was investigated via molecular dynamics (MD) simulations and density functional theory (DFT) calculations to confirm our hypothesis. The particular numbers of ions and molecules in the MD simulations box are summarized in Table S2. The snapshots of the simulated electrolyte structure (Figure 1a,c and Figure S3) along with the radial distribution functions (RDFs) and coordination number (CN) analyses (Figure 1b,d and Figure S4) revealed a pronounced ionic solvation cluster for Zn^{2+} coordinated with SO_4^{2-}, H_2O, and DMF. The RDFs of the $ZnSO_4$−H_2O electrolyte presented that the primary solvation shell of Zn^{2+} (central ion) was at a distance of ∼2.50 Å (Figure 1b). A distinct Zn−O (DMF) pair was observed at ∼1.88 Å after introducing DMF, implying that DMF could be incorporated into the Zn^{2+} solvation structure (Figure 1d and Figure S4). At an increased ratio of DMF and H_2O, the CN of H_2O in the solvation layer decreased from 3.82 to 3.48, whereas the CN of DMF increased from 0 to 0.44, indicating that DMF molecules are participating in the Zn^{2+} solvation structure (Figure S5 and Table S3). Additionally, new complexes of $Zn^{2+}[DMF]_1[H_2O]_4[SO_4^{2-}]_1$ and $Zn^{2+}[DMF]_2[H_2O]_3[SO_4^{2-}]_1$ were found in the hybrid electrolytes (Figure S6), which exhibited larger dissociation energies than the $Zn^{2+}[H_2O]_5[SO_4^{2-}]_1$ complex (Figure 1e). These results elucidate that the DMF molecules have a much stronger affinity to the Zn^{2+} and may significantly change the Zn^{2+} solvation structure. Meanwhile, the content of $Zn^{2+}[H_2O]_5[SO_4^{2-}]_1$ complex also decreased from 65.4% in $ZnSO_4$−H_2O to 51.4% in $ZnSO_4$−H_2O−DMF (5:1) and 39.6% in $ZnSO_4$−H_2O−DMF (4:2), respectively (Figure S6).

https://doi.org/10.1021/acsenergylett.3c00154
ACS Energy Lett. 2023, 8, 1613−1625

Furthermore, the relative binding energies of Zn^{2+} to other species could be ranked in the following sequence: Zn^{2+}–SO_4^{2-} > Zn^{2+}–DMF > Zn^{2+}–H_2O, suggesting that Zn^{2+} preferentially coordinates with DMF rather than H_2O (Figure 1f). Hence, the decreased number of coordinating H_2O and free H_2O (Figure S7) implies a lower possibility for the occurrence of side reactions (*e.g.*, HER) during the Zn deposition process.

Various spectroscopic analyses, including nuclear magnetic resonance (NMR), Raman spectroscopy, and Fourier transform infrared (FTIR) spectroscopy, were conducted to investigate the solvation structure of the hybrid electrolytes and the interaction between $ZnSO_4$ and the solvents. As shown in Figure 1g, the ^1H peak of pure H_2O centered at 4.70 ppm and shifted to 4.73 ppm after dissolving $ZnSO_4$ into an aqueous solution. Notably, the ^1H peak further moved to 4.89 ppm in $ZnSO_4$–H_2O–DMF when DMF was added. These results indicate that the deshielding by DMF decreased the electron cloud density around ^1H from H_2O, confirming the formation of HB between DMF and H_2O that weakened the solvation effect between Zn^{2+} and H_2O.[18] Moreover, the ^{17}O chemical shift in H_2O exhibited an upfield shift from 4.56 ppm in the $ZnSO_4$–H_2O electrolyte to 4.26 ppm in the $ZnSO_4$–H_2O–DMF electrolyte, supporting the possible incorporation of DMF into the modified solvation structure of Zn^{2+} with H_2O (Figure S8). The Raman spectra of H_2O were resolved into three bands centered at 3229, 3409, and 3554 cm^{-1}, which were attributed to be symmetric and asymmetric OH stretching and the free OH of water, respectively (Figure 1h).[25] Accordingly, the addition of DMF significantly broke the strong HB networks containing H_2O, which was confirmed by the weakened OH stretching. Consequently, the blue shift of C–H stretching of DMF was attributed to the reformation of the HB between the C=O group of DMF and H_2O molecules. The FTIR spectrum also demonstrated a discernible blueshift in the OH bending vibration at 1600–1700 cm^{-1} and a redshift in the OH stretching vibration at 3000–3500 cm^{-1} of H_2O as the DMF content increased, verifying the construction of modified HB networks between DMF and H_2O.[25] In addition, a blueshift in the C=O bending vibration of DMF (~1661 cm^{-1}) was observed in the hybrid electrolytes because of the HB between C=O and H_2O.

The above MD and DFT calculations and experimental results obtained through NMR, FTIR, and Raman spectroscopy demonstrate strong implications for the change in the Zn^{2+} solvation structure when incorporating DMF into the electrolyte. Additionally, the electrochemical stability windows of various electrolytes were investigated on nonactive stainsteel electrodes by linear sweep voltammetry (LSV), as shown in Figures 1i and S9. The $ZnSO_4$–H_2O electrolyte demonstrated a larger current response than the hybrid electrolytes, indicating the significant suppression of the HER and the OER (oxygen evolution reaction) by DMF addition owing to the reformation of the HB derived from the strong interaction between DMF and H_2O. In addition, the hybrid electrolyte also exhibits a nonflammable nature, further proving its practicability (Figure S10). Therefore, the DMF is expected to positively influence the electrodeposition behavior of Zn metal, which further enables new interface chemistry induced by DMF, as discussed below.

High Reversibility of Zn/Zn^{2+} and Uniform Zn Deposition. The stability and reversibility of the Zn anode in $ZnSO_4$–H_2O and $ZnSO_4$–H_2O–DMF electrolytes were evaluated at 1 mA cm^{-2} and 1 mA h cm^{-2} using symmetric Zn||Zn cells (Figure 2a and Figure S11). After the initial activation, the symmetric Zn||Zn cells in $ZnSO_4$–H_2O–DMF (H_2O:DMF = 5:1 and 4:2) electrolytes exhibited steady charge/discharge process over 1780 and 2500 h, respectively. By contrast, the Zn||Zn cell using $ZnSO_4$–H_2O electrolyte failed in doing after 92 h of cycling process because of an internal short circuit resulting from the Zn dendrites. Notably, the Zn||Zn symmetric cells in $ZnSO_4$–H_2O–DMF produced a higher voltage gap than those in $ZnSO_4$–H_2O, which was attributed to the stronger solvation effect and lower ion conductivity of hybrid electrolyte (Figure 1e and Figure S12). The $ZnSO_4$–H_2O–DMF (4:2) electrolyte was selected for evaluating the electrochemical performance at higher current densities due to the longer cycle life of the Zn||Zn cell than that in the $ZnSO_4$–H_2O–DMF (5:1) electrolyte. As shown in Figure S13 and Figure 2b, the Zn||Zn cell in the $ZnSO_4$–H_2O–DMF (4:2) electrolyte achieved stable operation for over 1400 h at 2 mA cm^{-2} and 1000 h at 4 mA cm^{-2}, respectively, with a specific capacity of 1 mA h cm^{-2}. Compared to the cycling performances of symmetric cells plotting the cumulative capacities of Zn||Zn cells as shown in Figure 2c (based on the data in Table S4), the cell with the $ZnSO_4$–H_2O–DMF electrolyte surpasses the values reported in previous studies at different current densities based on the electrolyte optimization strategies.[12,13,16−20,27−41] Figure 2d and Figure S14 illustrate the rate capability of the symmetric cells in hybrid and aqueous electrolytes at 1 mA h cm^{-2} and varying current rates from 0.5 to 10 mA cm^{-2}. Although the overpotential of the cells using the $ZnSO_4$–H_2O–DMF electrolyte was slightly larger than that obtained with the $ZnSO_4$–H_2O electrolyte, the former showed very stable voltage profiles up to 10 mA cm^{-2} and improved cycle life of over 1000 h than that of the latter. By contrast, short circuits at 4 mA cm^{-2} were observed for the cell in $ZnSO_4$–H_2O electrolyte after cycling at 1 and 2 mA cm^{-2}. Even at a more practical condiction (4 mA cm^{-2} and 4 mAh cm^{-2}), the hybrid electrolyte still promotes desirable Zn plating/stripping with high cycling stability and reversibility (Figure S15).

The performances of Zn||Zn symmetric cells in dilute aqueous and hybrid electrolytes at the fixed concentration of 0.3 M $ZnSO_4$ were compared to clarify the role of DMF.[42] A short circuit occurs in the symmetric cells after 54 h in the dilute $ZnSO_4$–H_2O electrolyte, while the cycle life was improved up to 400 h in the dilute $ZnSO_4$–H_2O–DMF electrolyte (Figure S16a). Bulky dendrites were formed in the dilute $ZnSO_4$–H_2O after 20 cycles, whereas a relatively smooth surface was observed in dilute $ZnSO_4$–H_2O–DMF (Figure S16b,c). These results indicate that the presence of DMF in hybrid electrolytes allows more reversible and dendrite-free Zn plating/stripping. Moreover, Zn||Cu asymmetric cells were employed to evaluate the Coulombic efficiency (CE) of Zn plating/stripping (Figure 2e). The Zn||Cu cells in hybrid electrolytes exhibit an enhanced average CE of 99.0% within initial cycles to 99.6%, owing to the formation of robust SEI. Stable voltage curves for Zn plating/stripping, wherein the separation of charge and discharge potentials initially decreased and stabilized at ~40 mV after 50 cycles, were observed in the $ZnSO_4$–H_2O–DMF electrolyte (Figure 2f). Conversely, the fluctuated CE values and unstable stripping profiles after 80 cycles were found in the $ZnSO_4$–H_2O electrolyte owing to dendrite formation, H_2 generation, and Zn corrosion (Figure S17).

https://doi.org/10.1021/acsenergylett.3c00154
ACS Energy Lett. 2023, 8, 1613−1625

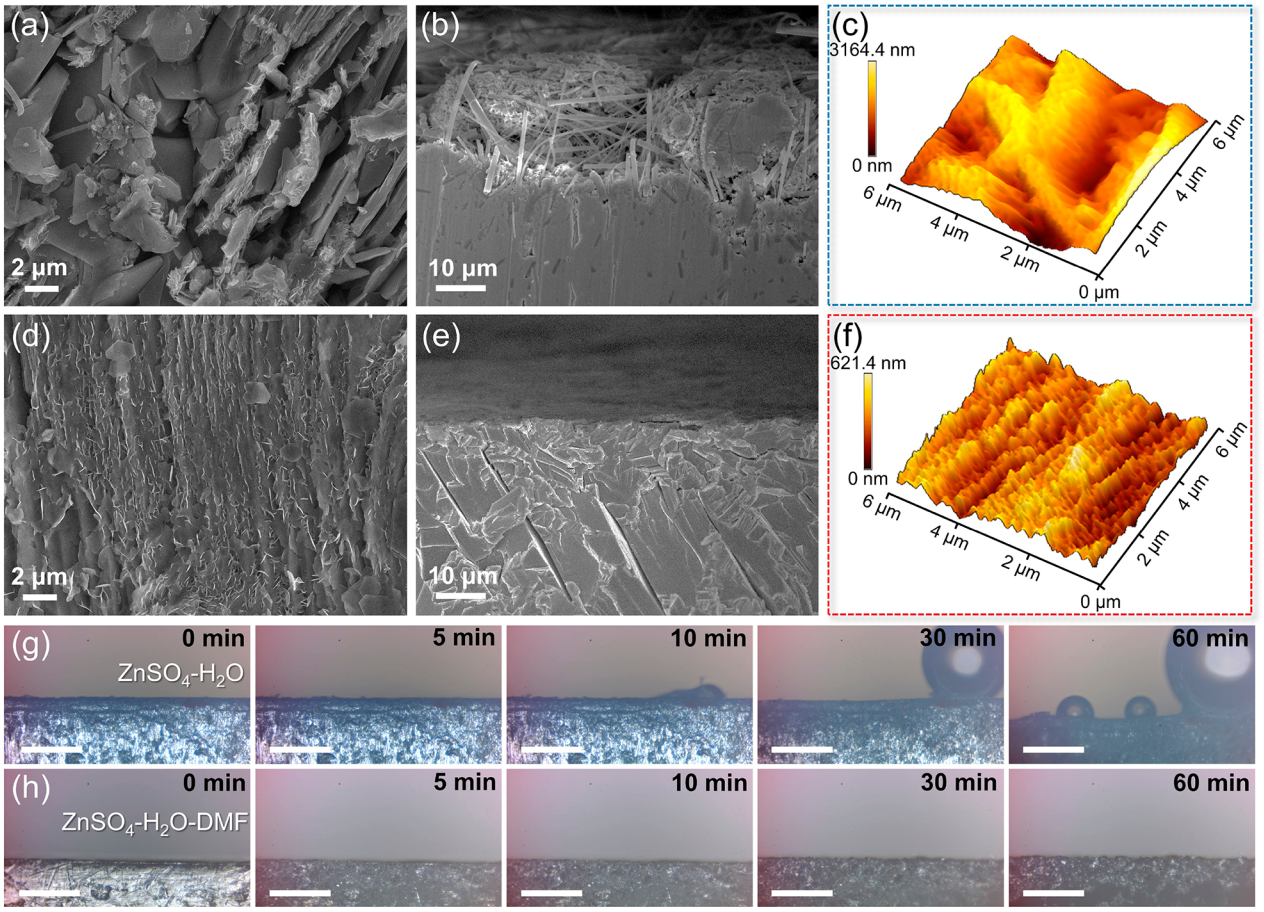

Figure 3. Comparison of Zn deposits in aqueous and hybrid electrolytes. SEM images of Zn anodes after 20 cycles in (a, b) $ZnSO_4$−H_2O and (d, e) $ZnSO_4$−H_2O−DMF. AFM images of Zn anodes after 20 cycles in (c) $ZnSO_4$−H_2O and (f) $ZnSO_4$−H_2O−DMF. Operando optical images of Zn anodes in (g) $ZnSO_4$−H_2O and (h) $ZnSO_4$−H_2O−DMF observed in symmetric transparent cells cycled at 10 mA cm^{-2} (the scale bar is 200 μm in each image). .

The suppression of the corrosion reaction of Zn in the hybrid electrolyte strongly influenced the significantly improved performance of Zn anodes. The Zn metal in $ZnSO_4$−H_2O−DMF electrolytes exhibited a more positive corrosion potential and lower corrosion current than those obtained using $ZnSO_4$−H_2O electrolyte, indicating a less tendency of corrosion reactions and a lower corrosion rate of the Zn electrode in the hybrid electrolyte (Figure S18). When the Zn foil was immersed in different electrolytes for 5 days, no apparent change was observed in the $ZnSO_4$−H_2O−DMF electrolyte, whereas numerous scattered flakes were observed in the $ZnSO_4$−H_2O electrolyte (Figures S19 and S20). As shown in the X-ray diffraction (XRD) patterns of the immersed Zn foils in different electrolytes (Figure S21), the corrosion byproduct ($Zn_4SO_4(OH)_6{\cdot}3H_2O$) is detected in the $ZnSO_4$−H_2O electrolyte. The pure Zn phase was only captured in hybrid electrolytes, confirming their anticorrosion effect. The Zn||Zn symmetric cell cycled in the hybrid electrolyte exhibited a more stable interface, which was supported by the facilitated interfacial charge-transfer kinetics indicated by the Nyquist plots during cycles (Figures 2g,h). Accordingly, the charge-transfer resistance (R_{ct}) of the Zn||Zn cells, derived from the semicircles in the high-frequency region, was lower in the $ZnSO_4$−H_2O−DMF electrolyte than that in the $ZnSO_4$−H_2O electrolyte (Table S5). Moreover, the initial R_{ct} values of the symmetric cells after 30 min were gradually reduced after 10 and 20 cycles at 1 mA cm^{-2} and 1 mA h cm^{-2} in both electrolytes owing to the better contact between Zn anodes and electrolyte during cycling (Figures 2g,h). The high Zn^{2+}-ion conductivity of *in situ* formed SEI and the enhanced wettability of Zn foil in the hybrid electrolyte are beneficial for reducing the R_{ct} and Gibbs free energy of the nucleation during the repeat Zn stripping/plating processes (insets of Figure 2g,h).[27]

Zn deposition morphologies and cross-sectional views in different electrolytes were analyzed using scanning electron microscopy (SEM) and atomic force microscopy (AFM) to confirm the inhibition effect of the hybrid electrolyte on Zn dendrite growth. The Zn surface in the $ZnSO_4$−H_2O electrolyte became rough with numerous protrusions (dendrites) and scattered flakes (corrosion products) along with a contact angle of 48.4° after 20 cycles at 1 mA cm^{-2} and 1 mA h cm^{-2} (Figures 3a and 3b and inset of Figure 2g). A smooth dendrite-free morphology and contact angle of ∼0° were obtained for Zn cycled in the $ZnSO_4$−H_2O−DMF electrolyte (Figures 3d and 3e and inset of Figure 2h). In particular, the AFM altitude intercept of the Zn foil cycled in the $ZnSO_4$−H_2O−DMF electrolyte (621.4 nm) was lower than that cycled in the $ZnSO_4$−H_2O electrolyte (3164.4 nm), which was consistent with the SEM results (Figure 3c,f). Direct evidence for the regulation of Zn plating through DMF addition was obtained from *in situ* optical visualizations (Movies S1 and

https://doi.org/10.1021/acsenergylett.3c00154
ACS Energy Lett. 2023, 8, 1613−1625

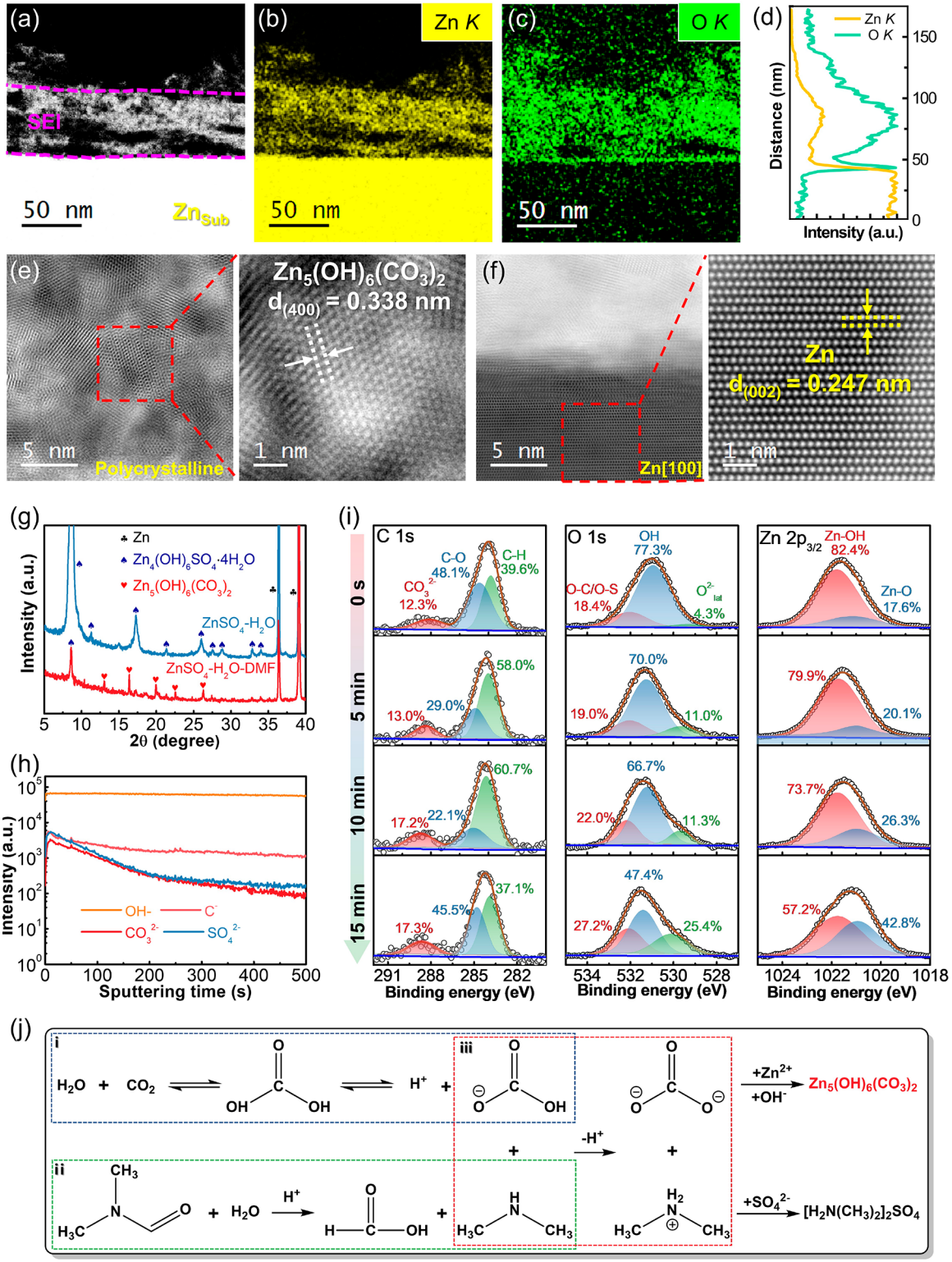

Figure 4. Structure and formation mechanism of the *in situ* formed SEI. (a) HAADF cross-sectional STEM image of the Zn anode surface after 20 cycles in $ZnSO_4$−H_2O−DMF. (b, c) EDX elemental maps of Zn *K* (8.630 keV) and O *K* (0.525 keV) peaks for the heterostructure. (d) EELS elemental profiles of Zn K and O K edges obtained across the interphase. (e, f) High-resolution ABF-STEM (left) and HAADF-STEM images of the polycrystalline SEI layer and single crystalline Zn anode, respectively. (g) XRD patterns of Zn anodes after 20 cycles in $ZnSO_4$−H_2O and $ZnSO_4$−H_2O−DMF. (h) TOF-SIMS and (i) in-depth XPS analysis of Zn anode surface after 20 cycles in $ZnSO_4$−H_2O−DMF. (j) Formation mechanism of proposed $Zn_5(OH)_6(CO_3)_2$-contained SEI. .

S2)., The relatively flat Zn surface in the $ZnSO_4$−H_2O electrolyte in the initial state became uneven and odd after 10 min of deposition at 10 mA cm^{-2}, along with a discernible gas bubble on the surface (Figure 3g and Movie S1). In contrast, uniform and compact Zn deposition without dendrite formation was observed for the Zn foil in the $ZnSO_4$−H_2O−

https://doi.org/10.1021/acsenergylett.3c00154
ACS Energy Lett. 2023, 8, 1613−1625

DMF electrolyte under the same condition for over 60 min (Figure 3h and Movie S2). To understand the Zn deposition behaviors further in different electrolytes, cyclic voltammetry (CV) and chronoamperometry (CA) characterizations were conducted in Zn||Ti and Zn||Zn symmetric cells, respectively. The nucleation overpotential in the $ZnSO_4$−H_2O−DMF electrolyte was ∼120 mV, which is higher than that in the $ZnSO_4$−H_2O electrolyte (Figure S22). The increased nucleation overpotential was attributed to the strong solvation of Zn^{2+} in the hybrid electrolyte, as revealed by the DFT calculation (Figure 1e). The activation energy in $ZnSO_4$−H_2O−DMF was 66.0 kJ mol^{-1}, which was derived from the Arrhenius equation. The obtained value is higher than that in $ZnSO_4$−H_2O (58.0 kJ mol^{-1}), indicating a higher energy barrier of Zn^{2+} deposition in the hybrid electrolyte in accordance with the theoretical calculations (Figure S23).[43] Considering that the high nucleation overpotential is associated with the fine-grained Zn deposits,[44] a smaller critical nucleus size for Zn deposition was predicted in the hybrid electrolyte, which was confirmed experimentally and theoretically. The CA test verified that the deposition model in the $ZnSO_4$−H_2O electrolyte corresponded to a long and extensive 2D ion diffusion process and rough deposition propagation, showing a continuous increase in the current density for more than 800 s at a constant potential of −150 mV (Figure S24). In contrast, the CA profile in the $ZnSO_4$−H_2O−DMF electrolyte was fitted with a relatively stable 3D diffusion process after 200 s of planar diffusion and nucleation, indicating short and placid diffusion and smooth Zn deposition.[44]

Structure and Formation Mechanism of the *In Situ* Formed SEI. The SEI *in situ* formed by the addition of DMF was investigated using transmission electron microscopy (TEM), XRD, and FTIR spectroscopy. All Zn samples were obtained after 20 cycles at 1 mA cm^{-2} and 1 mA h cm^{-2}. The high-angle annular dark field (HAADF) cross-sectional scanning TEM (STEM) image in Figure 4a shows an obvious SEI layer with a thickness of 60−70 nm on the Zn surface cycled in the $ZnSO_4$−H_2O−DMF electrolyte, which serves as an electronically insulating barrier that restricted water decomposition and an ionically conducting layer for the uniform Zn^{2+} flux. Additionally, the combined element profiles obtained from electron energy loss spectroscopy (EELS) and elementary maps of energy dispersive X-ray spectroscopy (EDX) revealed that the Zn signal of the SEI was weaker than that from the bulk region of Zn, whereas the O signal was much stronger in the SEI region (Figure 4b−d), indicating the different chemical identities of the less dense SEI and metallic Zn anode. Based on the EELS plasmon-loss mapping of the SEI ($E_{p,SEI}$ = 19.2 eV)/Zn ($E_{p,Zn}$ = 13.5 eV) heterostructure (Figure S25a−c), the two regions are distinctively resolved, implying that the SEI and Zn are electronically different phases. Furthermore, high-resolution annular bright field (ABF) and HAADF STEM images demonstrate that the composition of the $Zn_5(OH)_6(CO_3)_2$ SEI layer, which consisted of polycrystalline structures aggregated by nanocrystals with a *d* spacing of 0.338 nm corresponding to the (400) plane of the $Zn_5(OH)_6(CO_3)_2$ phase (Figure 4e). In contrast, as shown in Figure 4f, the Zn anode exhibited a typical lattice fringe of Zn (002). This SEI was absent from the $ZnSO_4$−H_2O electrolyte (Figure S26), and a $Zn_4SO_4(OH)_6{\cdot}4H_2O$ byproduct was formed instead on the Zn surface in the $ZnSO_4$−H_2O electrolyte, as shown in the XRD analysis of the cycled Zn foil (Figure 4g and Figure S27). Despite the negligible presence of the byproduct ($Zn_4SO_4(OH)_6{\cdot}4H_2O$), the characteristic peaks of $Zn_5(OH)_6(CO_3)_2$ were dominant on the Zn foil in the $ZnSO_4$−H_2O−DMF electrolyte (Figure 4g). Consequently, a chemically, electronically, and crystallographically independent $Zn_5(OH)_6(CO_3)_2$ SEI, which was different from metallic Zn phase, was *in situ* formed in hybrid electrolytes.

The chemical structure of SEI formed in the $ZnSO_4$−H_2O−DMF electrolyte was further characterized using the time-of-fight secondary ion mass spectrometry (TOF-SIMS) and in-depth X-ray photoelectron spectroscopy (XPS). As shown in Figure 4h, OH^- (m/e = 17), CO_3^{2-} (m/e = 60), and C^- (m/e = 12, originating from the decomposition of CO_3^{2-}) signals were found at various sputtering depths in the negative mode, implying the existence of $Zn_5(OH)_6(CO_3)_2$ in the SEI. This result was also supported by the FTIR spectra in Figure S28, indicating a large amount of CO_3^{2-} (∼1500 cm^{-1}) and OH^- (∼3800 cm^{-1}) in the SEI region for the Zn foil cycled in the $ZnSO_4$−H_2O−DMF electrolyte.[45] An in-depth XPS with argon sputtering was also conducted to analyze the chemical composition and element depth distribution in SEI. The C atom signal, as an indicator of CO_3^{2-}, was stronger than that of S atom (an indicator of SO_4^{2-}) at various etching times (Figure S29). A minor CO_3^{2-} species (12.3%) was detected on the SEI surface (before etching) in the $ZnSO_4$−H_2O−DMF electrolyte, as verified by the C 1s spectra in Figure 4i. After etching the surface with Ar^+ bombardment, the ratio of CO_3^{2-} increased to 17.2% after 10 min and remained saturated up to 15 min, implying the formation of a CO_3^{2-}-containing interphase. This resistance to etching may be attributed to the very dense SEI layer. Furthermore, the formation of CO_3^{2-} was confirmed using the O−C/O−S signal in the O 1s spectra at different etching stages (O 1s spectrum in Figure 4i). In addition, the SEI contains a large amount of Zn−OH and a small amount of Zn−O, as observed in the Zn $2p_{3/2}$ spectrum, which is consistent with the distribution of OH and $O^{2-}_{lattice}$ signals in the O 1s spectrum.

The formation process of $Zn_5(OH)_6(CO_3)_2$ is proposed in Figure 4j. Because CO_3^{2-} was absent in the electrolyte salt of $ZnSO_4$, CO_3^{2-} species were formed from the dissolved CO_2 in electrolytes, contributing to the formation of $Zn_5(OH)_6(CO_3)_2$. Initially, the dissolved CO_2 and H_2O in the $ZnSO_4$−H_2O−DMF electrolyte attain equilibrium in stage i.[46] Subsequently, the hydrolysis of DMF in stage ii easily occurs due to the acidic nature of the electrolyte, producing formic acid (HCOOH) and dimethylamine ($(CH_3)_2NH$) while increasing pH value (Figures S30−S33).[47,48] In stage iii, the dimethylamine spontaneously reacts with HCO_3^- in an aqueous environment, leading to the production of CO_3^{2-} species through the deprotonation of bicarbonate as previously demonstrated.[49] Finally, CO_3^{2-} species react with Zn^{2+} and OH^- to form $Zn_5(OH)_6(CO_3)_2$, which is solidified due to its low solubility in electrolyte solutions and aggregated into polycrystalline structures. Therefore, the three-stage reactions can be combined into the overall reaction: $2HCON(CH_3)_2 + 2CO_2 + 2H_2O + ZnSO_4 + 4Zn(OH)_2 \rightarrow Zn_5(OH)_6(CO_3)_2\downarrow + [H_2N(CH_3)_2]_2SO_4 + 2HCOOH$. The total energies of reactants and products in the reaction were estimated through DFT theoretical calculation (Figure S34). Consequently, the calculated reaction energy was −7.78 eV/$Zn_5(OH)_6(CO_3)_2$, indicating a thermodynamically spontaneous reaction.

https://doi.org/10.1021/acsenergylett.3c00154
ACS Energy Lett. 2023, 8, 1613−1625

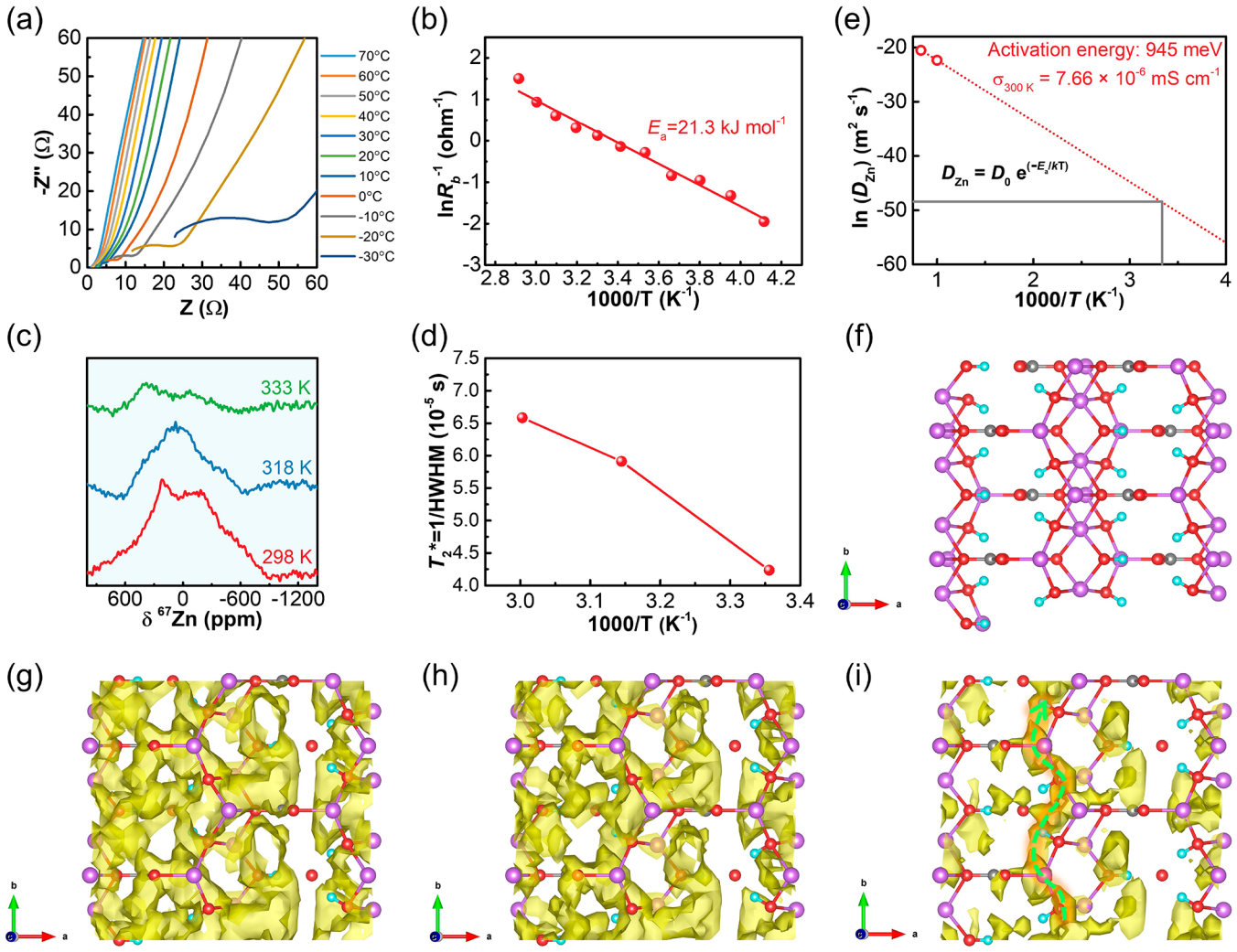

Figure 5. Zn^{2+} ion transport of the *in situ* formed SEI over a wide temperature range. (a) Nyquist plots of $Zn_5(OH)_6(CO_3)_2$ coated Ti symmetric cell with glass fiber as separator tested at open circuit voltage (OCV) over the frequency range of 100 kHz to 1 Hz. (b) Arrhenius behavior of the reciprocal resistances corresponding to interfacial components and the activation energy derived for the $Zn_5(OH)_6(CO_3)_2$ film. (c) Stack plot of ^{67}Zn NMR spectra at various temperature of $Zn_5(OH)_6(CO_3)_2$ collected at 11.7 T corresponding to Larmor frequencies of 31.290 MHz. (d) Temperature dependence of the T_2* extracted from the NMR relaxometry study. (e) Arrhenius plot based on predicted D_{Zn} values in $Zn_5(OH)_6(CO_3)_2$ from AIMD simulations. (f) Crystal structure of $Zn_5(OH)_6(CO_3)_2$ along with [001] lattice plane. Zn, C, O, and H are colored purple, gray, red, and cyan, respectively. (g–i) Zn^{2+} probability density from AIMD at 1200 K, and the isosurfaces are plotted at 0.001, 0.002, and 0.005 Bohr^{-3}, respectively. .

Zn^{2+} Ion Transport of the In Situ Formed SEI over a Wide Temperature Range. To understand the Zn^{2+}-ion conduction behavior in SEI, we synthesized the sheet-like $Zn_5(OH)_6(CO_3)_2$ compounds via a facile precipitation method[50] and characterized them using SEM and XRD (Figure S35). The $Zn_5(OH)_6(CO_3)_2$ film demonstrated an increase in the ionic conductivity from 0.04 to 1.27 mS cm^{-1} in a temperature range from −30 to 70 °C (Figures S36 and S37 and Figure 5a). The effective Zn^{2+} diffusion through the $Zn_5(OH)_6(CO_3)_2$ phase was confirmed estimating the low activation energy of 21.3 kJ mol^{-1} obtained from Arrhenius plot (Figure 5b), which is lower than that of an inorganic solid Zn-ion conductor (*e.g.*, 57.9 kJ mol^{-1} for a TiO_2-based solid-state electrolyte).[51] Notably, we first applied solid-state ^{67}Zn NMR relaxometry to reveal the local environment and dynamics of Zn^{2+} ions and their mobility within the $Zn_5(OH)_6(CO_3)_2$ phase at 298, 318, and 333 K (Figure 5c). The transverse (or spin−spin) relaxation time (T_2*), which is inversely proportional to the full width at half-maximum (FWHM) of the NMR peaks, is closely correlated with the Zn^{2+}-ion mobility of the solid-state $Zn_5(OH)_6(CO_3)_2$; this is because high ionic mobility can average the anisotropic dipolar and quadrupolar interactions.[52] The calculation of T_2* from the broad peak of ^{67}Zn NMR at various temperatures (Figure 5d) suggested that an increase in temperature improves Zn-ion mobility. This provides direct evidence for the motion of Zn^{2+} ions in the $Zn_5(OH)_6(CO_3)_2$ structure, which can function as a Zn^{2+}-ion conducting, *in situ* formed SEI in AZMBs.

DFT-based *ab initio* MD (AIMD) simulations were performed to predict the diffusivity of Zn (D_{Zn}) in $Zn_5(OH)_6(CO_3)_2$ at 300 K.[53] As shown in Figure S38a,b, the mean-square displacements of Zn atoms were calculated at a given temperature (1000 and 1200 K). After disregarding the first 2 ps, we estimated the D_{Zn} values from the linear fits and constructed an Arrhenius plot of ln(D_{Zn}) versus 1000/T based on D_{Zn} at different temperatures (Figure 5e). The activation barrier was predicted to be 945 meV, which is lower than the reported value for the Zn^{2+} conductor ($ZnZr_4(PO_4)_6$, 1300

https://doi.org/10.1021/acsenergylett.3c00154
ACS Energy Lett. 2023, 8, 1613−1625

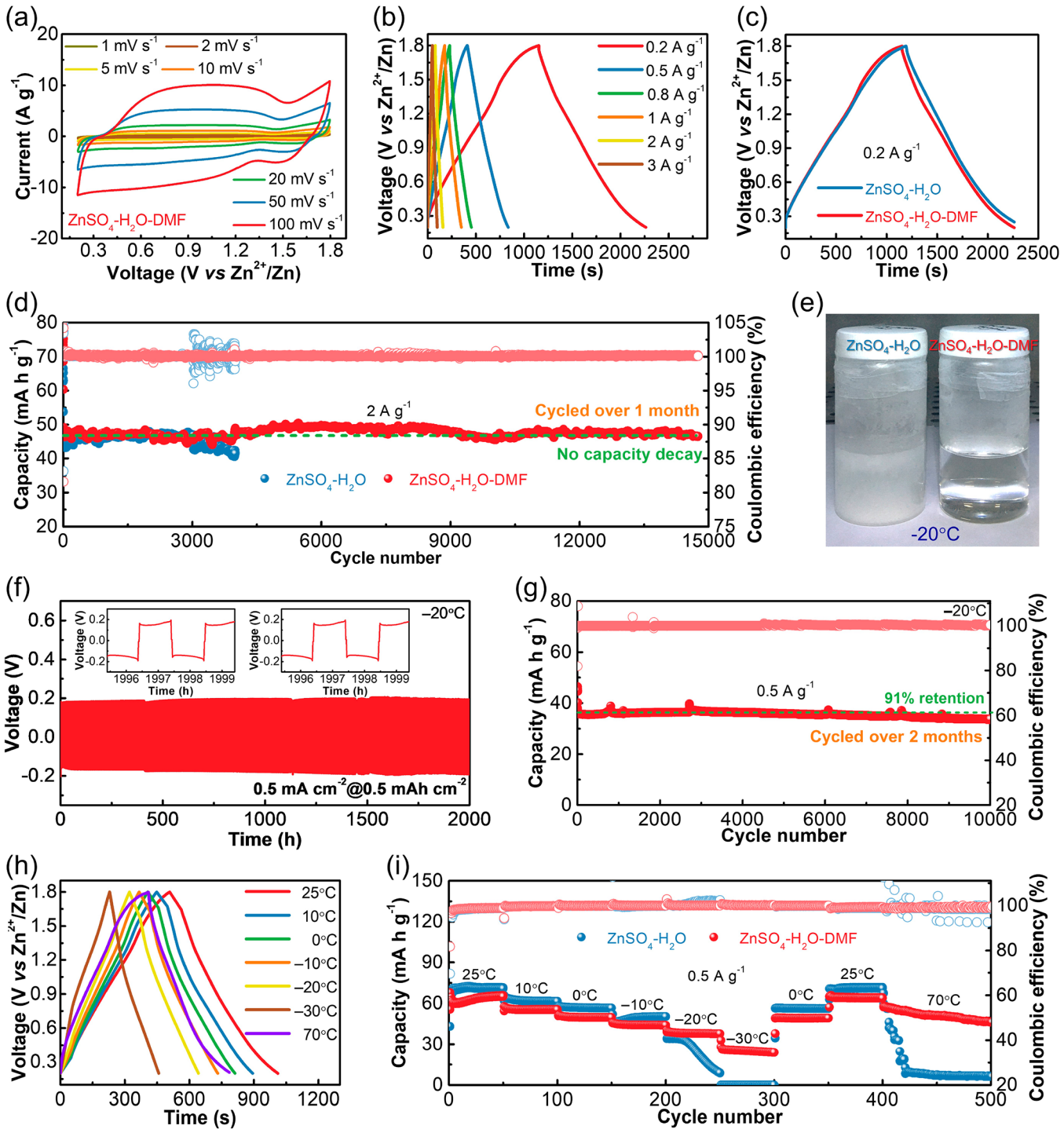

Figure 6. Electrochemical performances of HZICs in hybrid electrolytes over a wide temperature range. (a) CV curves of HZICs in $ZnSO_4$−H_2O−DMF at different scan rates. (b) Galvanostatic charge−discharge profiles of HZICs in $ZnSO_4$−H_2O−DMF at various current densities. (c) Galvanostatic charge−discharge profiles of HZICs in different electrolytes at 0.2 A g^{-1}. (d) Cycling performance of HZICs with different electrolytes at 2 A g^{-1}. (e) The physical state of $ZnSO_4$−H_2O and $ZnSO_4$−H_2O−DMF electrolytes at −20 °C. cycling performance of (f) Zn‖Zn symmetric cell at 0.5 mA cm^{-2} and 0.5 mA h cm^{-2} and (g) HZICs at 0.5 A g^{-1} in $ZnSO_4$−H_2O−DMF. (h) Galvanostatic charge−discharge profiles in $ZnSO_4$−H_2O−DMF tested at 0.5 A g^{-1} and various temperatures. (i) The temperature fluctuation test for HZICs at 0.5 A g^{-1}.

meV)[54] and comparable to various Zn conductors proposed theoretically.[55] In addition, the crystal structure of $Zn_5(OH)_6(CO_3)_2$ along the [001] lattice plane and the Zn^{2+} probability density isosurfaces from the AIMD simulation at 1200K are shown in Figure 5f−i. When the isosurface was increased to 0.005 $Bohr^{-3}$, the Zn^{2+} probability density was still continuous along the [010] lattice plane, as indicated by the green arrow in Figure 5i. This suggests that most of the Zn^{2+} migration in the $Zn_5(OH)_6(CO_3)_2$ phase occurs along the [010] lattice plane. The Zn-ion conductivity of $Zn_5(OH)_6(CO_3)_2$ at 300 K ($\sigma_{300\ K}$) could be extrapolated as 7.66×10^{-6} mS cm^{-1}. Although the value is lower than that of

https://doi.org/10.1021/acsenergylett.3c00154
ACS Energy Lett. 2023, 8, 1613−1625

single-ion conductor $ZnPS_3$ ($\sigma = 10^{-5}$ to 10^{-3} mS cm^{-1} at 60 °C),[56] it is still higher than that of Li_2CO_3 (3.58×10^{-7} mS cm^{-1})[57] and LiF ($\approx 10^{-28}$ mS cm^{-1}),[58] which were identified as the major components of SEI in LIBs. Even though LiF exhibits ionic insulation property, Li-ions can still diffuse through the grain boundary (GB) formed between LiF and other inorganic compounds (Li_2CO_3 and Li_2O) in the SEI.[59,60] In our study, considering that $Zn_5(OH)_6(CO_3)_2$ was generated in the form of polycrystalline as shown in Figure 4e, the GB was formed between polycrystalline grains. Given by the ionic conductivity difference between polycrystalline $Zn_5(OH)_6(CO_3)_2$ film and single crystalline $Zn_5(OH)_6(CO_3)_2$ phase determined experimentally and theoretically, respectively, Zn-ions could travel through the $Zn_5(OH)_6(CO_3)_2$-contained interphases. Hence, the $Zn_5(OH)_6(CO_3)_2$-contained interphase rather than the $Zn_5(OH)_6(CO_3)_2$ itself is suggested that the main beneficiary of Zn^{2+}-ion transport. The fast transport of Zn^{2+} was guided by the interfacial layer, which was confirmed by the decreased R_{ct} in the hybrid electrolyte (Table S5).

Extremely Stable and Highly Efficient Hybrid Zn-Ion Capacitors over a Wide Temperature Range. Hybrid Zn-ion capacitors (HZICs) were fabricated by coupling Zn negative electrodes with commercial active carbon (AC) positive electrodes to clarify the superiority of our hybrid electrolyte for practical application (Figure 6). For comparison, the electrochemical performance of HZICs with $ZnSO_4$−H_2O electrolyte was evaluated under the same condition. The CV curves and galvanostatic charge−discharge (GCD) profiles show that both HZICs in the two electrolytes exhibit typical Faradaic features originating from the stripping/plating process of Zn/Zn^{2+} (Figure 6a,b and Figure S39). The specific capacity and IR drop of HZICs in $ZnSO_4$−H_2O−DMF were nearly comparable to those of $ZnSO_4$−H_2O at 0.2 A g^{-1} despite the lower ion conductivity (Figure 6c and Figure S12). However, the cycling performance significantly improved in hybrid electrolytes. As shown in Figure 6d, the HZICs in $ZnSO_4$−H_2O−DMF demonstrated long-term stability over 14,000 cycles (over 1 month) with a CE of approximately 100% at a high current density of 2 A g^{-1}. Conversely, the capacity decay was severe in $ZnSO_4$−H_2O, and the CEs rapidly reduced after 3000 cycles, indicating the formation of dead Zn. As demonstrated by the morphology of the Zn anodes after 500 cycles in SEM analysis (Figure S40), massive protrusions were observed on the Zn anode cycled in $ZnSO_4$−H_2O, while a smooth dendrite- or void-free surface was obtained in $ZnSO_4$−H_2O−DMF. Moreover, a thin Zn anode (~20 μm, ≈11.7 mA h cm^{-2}) and high mass loading AC electrode (~42 mg cm^{-2}) were used in the HZICs to realistically evaluate the performance of the Zn anode under high depth of discharge (DOD) values. As shown in Figure S41, the HZICs exhibited a high capacity of 42 mA h g^{-1} at 0.5 A g^{-1}, corresponding to an areal capacity of 1.76 mA h cm^{-2}. Thus, the DOD was calculated to be ~15%. As expected, the HZICs also showed stable cycle performance of over 5000 cycles in $ZnSO_4$−H_2O−DMF, which was better than that in $ZnSO_4$−H_2O.

Compared to other solvent additives, such as dimethyl sulfoxide and acetonitrile, DMF shows a relatively lower freezing point of −61 °C.[22] Considering that DMF destroyed the HBs in $ZnSO_4$−H_2O−DMF, the hybrid electrolyte is expected to provide an antifreezing characteristics at low temperatures.[61] $ZnSO_4$−H_2O froze at −11 °C, whereas the freezing points of the hybrid electrolytes decreased to −18 °C and −32 °C for $ZnSO_4$−H_2O−DMF with H_2O/DMF ratios of 5:1 and 4:2, respectively (Figure S42). The temperature-dependent ionic conductivities confirmed that the conductivity values of $ZnSO_4$−H_2O−DMF (2.8 mS cm^{-1}) and $ZnSO_4$−H_2O (1.5 mS cm^{-1}) were reversed at −20 °C (Figure S43). The digital photos in Figure 6e indicate that the abrupt decrease in ionic conductivity is caused by the freezing of $ZnSO_4$−H_2O at −20 °C. In contrast, the liquid state was preserved for $ZnSO_4$−H_2O−DMF with high ionic conductivity. Accordingly, voltage profiles for Zn||Zn symmetric cells in $ZnSO_4$−H_2O−DMF were very stable over 2000 h at −20 °C (Figure 6f). Even at −20 °C, the HZICs reached a high capacity retention of 99% after 10,000 cycles (over 2 months), along with high CEs of approximately 100% (Figure 6g).

In addition to low-temperature operation, the high-temperature operation in $ZnSO_4$−H_2O−DMF should be considered toward all-climate applications. The addition of DMF strengthened the thermal stability of $ZnSO_4$−H_2O because of the inhibited evaporation of H_2O owing to the strong interaction between DMF and H_2O, as confirmed by the DSC test from 25 to 150 °C (Figure S44). At 60 °C, the HZICs using a hybrid electrolyte exhibit a higher reversible capacity of 38.4 mA h g^{-1} after 1000 cycles at 2 A g^{-1}, while the cells cycled in $ZnSO_4$−H_2O failed after 570 cycles (Figure S45). Even at a high temperature of 70 °C, the HZICs could be operated satisfactorily in $ZnSO_4$−H_2O−DMF over 600 cycles; however, the capacity in $ZnSO_4$−H_2O abruptly reduced to near zero after 20 cycles (Figure S46). When the water in the $ZnSO_4$−H_2O electrolyte evaporates at high temperatures, solubility in the electrolyte decreases for salt precipitation, and chemical activity increases, causing undesirable reactions and hence the degradation of the cyclic stability and capacity of HZICs.[10] Moreover, the HZICs with the $ZnSO_4$−H_2O−DMF electrolyte were very tolerant of operating over a wide range of temperatures from −30 to 70 °C (Figure 6h,i). During the temperature fluctuation, the capacities of HZICs in $ZnSO_4$−H_2O abruptly dropped from −20 to 70 °C, while those in hybrid electrolytes became considerably higher. The CEs of the HZICs in the hybrid electrolytes were ≈100%, while cell failure was observed in DMF-free electrolyte when cycled at −30 and 70 °C (Figure 6i and Figure S47). To the best of our knowledge, this is the first report of Zn metal anode in liquid electrolytes achieving outstanding performances and stabilities over a wide range of extreme temperatures.

Electrochemical impedance spectroscopy was conducted on the Zn||Zn symmetric cells after 20 cycles at −20 and 70 °C with a current of 1 mA cm^{-2} and a capacity of 1 mA h cm^{-2} to investigate the stability of the Zn anode-electrolyte interphase at low and high temperatures (Figure S48 and Table S6). Notably, the first semicircle (R_{int}) is associated with ion adsorption and desorption on the SEI in the high-frequency region, and the other is attributed to the R_{ct} in the medium-frequency region.[18] The R_{int} can be fitted with 3077 (at −20 °C) and 8.9 Ω (at 70 °C), corresponding to an ion conductivity of $1.1-1.3 \times 10^{-6}$ and $3.8-4.4 \times 10^{-4}$ mS cm^{-1}, respectively, resulting in uniform Zn flux and deposition through SEI layers. Thermogravimetry analysis (TGA) was performed to evaluate the thermal stability of SEI (Figure S49). The weight loss below 200 °C occurred owing to the evaporation of adsorbed water, and one endothermic peak was observed at approximately 250 °C, indicating the thermal decomposition of $Zn_5(OH)_6(CO_3)_2$ ($Zn_5(OH)_6(CO_3)_2 \rightarrow 5ZnO + 2CO_2 + 3H_2O$[50]). This decomposition temperature is

https://doi.org/10.1021/acsenergylett.3c00154
ACS Energy Lett. 2023, 8, 1613−1625

far beyond the operating temperature of the HZIC at 70 °C, confirming an outstanding interfacial thermal stability. Therefore, the wide-range temperature-tolerant electrochemical performances of HZIC cells in hybrid electrolytes can be attributed to the modified solvated structure and the newly formed $Zn_5(OH)_6(CO_3)_2$ SEIs of the hybrid electrolyte, which leads to thermal stability at high temperatures and high ion conductivity at low temperatures.

In summary, we developed new electrolyte chemistry for Zn metal batteries by adding DMF as a cosolvent in the electrolyte, thus manipulating the solvation structure of Zn^{2+} and SEI formation. The experimental and simulation analysis results suggested that the intensified HB of DMF-H_2O and weakened solvation interaction of Zn^{2+} with H_2O were realized by the strong solvation effect between DMF and Zn^{2+}. This hybrid electrolyte featured a unique Zn^{2+} solvation structure and the *in situ* formation of a Zn^{2+}-conducting and robust $Zn_5(CO_3)_2(OH)_6$ SEI through three-stage reactions. Moreover, the formation and Zn^{2+} transport mechanisms of a Zn^{2+}-conducting and robust $Zn_5(CO_3)_2(OH)_6$ were also comprehensively analyzed using spectroscopic and electrochemical characterizations and computational calculations. As a result, this hybrid electrolyte could effectively suppress the parasitic reactions and facilitate interfacial charge transfer through $Zn_5(CO_3)_2(OH)_6$ SEI. This enables highly reversible and dendrite-free Zn plating/stripping performance of over 2500 h operated at 25 °C (1 mA cm^{-2} and 1 mA h cm^{-2}) and 2000 h operated at −20 °C (0.5 mA cm^{-2} and 0.5 mA h cm^{-2}) in the Zn||Zn symmetric cells. In addition, the superiority of this hybrid electrolyte was confirmed demonstrating a high capacity of 42 mA h g^{-1} at 0.5 A g^{-1} and long-term cyclic stabilities and high CEs in the range of −20 to 70 °C for HZIC full cells employing thin Zn (∼20 μm) and high mass loading AC electrodes (∼42 mg cm^{-2}). Therefore, this study not only proposes a simple but effective electrolyte modification approach to achieve dendrite-free Zn anodes for high-performance Zn-based energy storage devices operated at extreme temperatures, but also provides a fundamental understanding of the unique Zn^{2+} ion transport in *in situ* formed SEI. In addition, employing other salts (such as $Zn(CF_3SO_3)$ and $Zn(N(CF_3SO_2)_2)_2$) and ionic additives (such as Mn^{2+}) would be an effective way to improve ionic conductivity and lower nucleation overpotential of a newly developed hybrid electrolyte.[62,63]

■ ASSOCIATED CONTENT

Supporting Information

The Supporting Information is available free of charge at https://pubs.acs.org/doi/10.1021/acsenergylett.3c00154.

Experimental Procedures, supporting figures (Figure S1−S49) and tables (Table S1−S6) on materials characterization and electrochemical measurement (PDF)

Movie S1: Operando optical video of Zn anode observed in symmetric transparent cell with $ZnSO_4$−H_2O (MP4)

Movie S2: Operando optical video of Zn anode observed in symmetric transparent cell with $ZnSO_4$−H_2O−DMF (MP4)

■ AUTHOR INFORMATION

Corresponding Author

Ho Seok Park − *School of Chemical Engineering, Sungkyunkwan University, Suwon-si, Gyeonggi-do 16419, Republic of Korea; SKKU Advanced Institute of Nanotechnology (SAINT), College of Engineering & Department of Health Sciences and Technology, Samsung Advanced Institute for Health Sciences and Technology (SAIHST), Sungkyunkwan University, Suwon-si, Gyeonggi-do 16419, Republic of Korea; SKKU Institute of Energy Science and Technology (SIEST), Sungkyunkwan University, Jangan-gu, Suwon 440-746, Republic of Korea;* orcid.org/0000-0002-4424-4037; Email: phs0727@skku.edu

Authors

Peixun Xiong − *School of Chemical Engineering, Sungkyunkwan University, Suwon-si, Gyeonggi-do 16419, Republic of Korea;* orcid.org/0000-0003-0824-1784

Yingbo Kang − *School of Chemical Engineering, Sungkyunkwan University, Suwon-si, Gyeonggi-do 16419, Republic of Korea*

Nan Yao − *Beijing Key Laboratory of Green Chemical Reaction Engineering and Technology, Department of Chemical Engineering, Tsinghua University, Beijing 100084, China*

Xiang Chen − *Beijing Key Laboratory of Green Chemical Reaction Engineering and Technology, Department of Chemical Engineering, Tsinghua University, Beijing 100084, China;* orcid.org/0000-0002-7686-6308

Haiyan Mao − *Department of Chemical and Biomolecular Engineering, Department of Chemistry, University of California, Berkeley, Berkeley, California 94720, United States*

Woo-Sung Jang − *Department of Energy Science, Sungkyunkwan University (SKKU), Suwon 16419, Republic of Korea*

David M. Halat − *Department of Chemical and Biomolecular Engineering, Department of Chemistry, University of California, Berkeley, Berkeley, California 94720, United States;* orcid.org/0000-0002-0919-1689

Zhong-Heng Fu − *Beijing Key Laboratory of Green Chemical Reaction Engineering and Technology, Department of Chemical Engineering, Tsinghua University, Beijing 100084, China*

Min-Hyoung Jung − *Department of Energy Science, Sungkyunkwan University (SKKU), Suwon 16419, Republic of Korea*

Hu Young Jeong − *Graduate School of Semiconductor Materials and Devices Engineering, Ulsan National Institute of Science and Technology (UNIST), Ulsan 44919, Republic of Korea;* orcid.org/0000-0002-5550-5298

Young-Min Kim − *Department of Energy Science, Sungkyunkwan University (SKKU), Suwon 16419, Republic of Korea;* orcid.org/0000-0003-3220-9004

Jeffrey A. Reimer − *Department of Chemical and Biomolecular Engineering, Department of Chemistry, University of California, Berkeley, Berkeley, California 94720, United States*

Qiang Zhang − *Beijing Key Laboratory of Green Chemical Reaction Engineering and Technology, Department of Chemical Engineering, Tsinghua University, Beijing 100084, China;* orcid.org/0000-0002-3929-1541

Complete contact information is available at:

https://doi.org/10.1021/acsenergylett.3c00154
ACS Energy Lett. 2023, 8, 1613−1625

https://pubs.acs.org/10.1021/acsenergylett.3c00154

Author Contributions

P. Xiong designed the experiments, analyzed data, and wrote the paper. Y. Kang assisted with the material synthesis and characterizations. N. Yao, X. Chen, Z.-H. Fu, and Q. Zhang conducted the calculations. H. Mao, D. Halat, and J. A. Reimer did the ^{67}Zn NMR tests. W.-S. Jang, M.-H. Jung, H. Y. Jeong, and Y.-M. Kim performed the TEM measerements. H. S. Park conceived and supervised the project. All authors contributed to interpretation of the results.

Notes

The authors declare no competing financial interest.

■ ACKNOWLEDGMENTS

This research was supported by the financial support from the National Research Foundation of Korea (NRF) grant funded by the Korea government (MSIT) (NRF-2020R1A3B2079803, NRF-2020R1A2C1006207), Republic of Korea. The STEM facility's use was supported by Advanced Facility Center for Quantum Technology at SKKU.

■ REFERENCES

(1) Ma, L.; Schroeder, M.; Borodin, O.; Pollard, T.; Ding, M.; Wang, C.; Xu, K. Realizing high zinc reversibility in rechargeable batteries. *Nat. Energy* **2020**, *5*, 743−749.

(2) Liang, Y.; Dong, H.; Aurbach, D.; Yao, Y. Current status and future directions of multivalent metal-ion batteries. *Nat. Energy* **2020**, *5*, 646−656.

(3) Jia, X.; Liu, C.; Neale, Z.; Yang, J.; Cao, G. Active materials for aqueous zinc ion batteries: synthesis, crystal structure, morphology, and electrochemistry. *Chem. Rev.* **2020**, *120*, 7795−7866.

(4) Liang, G.; Zhu, J.; Yan, B.; Li, Q.; Chen, A.; Chen, Z.; Wang, X.; Xiong, B.; Fan, J.; Xu, J.; Zhi, C. Gradient fluorinated alloy to enable highly reversible Zn-metal anode chemistry. *Energy Environ. Sci.* **2022**, *15*, 1086−1096.

(5) Tang, B.; Shan, L.; Liang, S.; Zhou, J. Issues and opportunities facing aqueous zinc-ion batteries. *Energy Environ. Sci.* **2019**, *12*, 3288−3304.

(6) Xiong, P.; Zhang, Y.; Zhang, J.; Baek, S. H.; Zeng, L.; Yao, Y.; Park, H. S. Recent Progress of Artificial Interfacial Layers in Aqueous Zn Metal Batteries. *EnergyChem.* **2022**, *4*, 100076.

(7) Blanc, L.; Kundu, D.; Nazar, L. Scientific challenges for the implementation of Zn-ion batteries. *Joule* **2020**, *4*, 771−799.

(8) Li, Q.; Wang, D.; Yan, B.; Zhao, Y.; Fan, J.; Zhi, C. Dendrite Issues for Zinc Anodes in a Flexible Cell Configuration for Zinc-Based Wearable Energy-Storage Devices. *Angew. Chem., Int. Ed.* **2022**, *61*, No. e202202780.

(9) Zhang, Q.; Luan, J.; Tang, Y.; Ji, X.; Wang, H. Interfacial design of dendrite−free zinc anodes for aqueous zinc−ion batteries. *Angew. Chem., Int. Ed.* **2020**, *59*, 13180−13191.

(10) Wang, H.; Chen, Z.; Ji, Z.; Wang, P.; Wang, J.; Ling, W.; Huang, Y. Temperature adaptability issue of aqueous rechargeable batteries. *Mater. Today Energy* **2021**, *19*, 100577.

(11) Nian, Q.; Sun, T.; Liu, S.; Du, H.; Ren, X.; Tao, Z. Issues and opportunities on Low-Temperature Aqueous Batteries. *Chem. Eng. J.* **2021**, *423*, 130253.

(12) Wang, F.; Borodin, O.; Gao, T.; Fan, X.; Sun, W.; Han, F.; Faraone, A.; Dura, J. A.; Xu, K.; Wang, C. Highly reversible zinc metal anode for aqueous batteries. *Nat. Mater.* **2018**, *17*, 543−549.

(13) Bayaguud, A.; Luo, X.; Fu, Y.; Zhu, C. Cationic surfactant-type electrolyte additive enables three-dimensional dendrite-free zinc anode for stable zinc-ion batteries. *ACS Energy Lett.* **2020**, *5*, 3012−3020.

(14) Guo, X.; Zhang, Z.; Li, J.; Luo, N.; Chai, G.; Miller, T. S.; Lai, F.; Shearing, P.; Brett, D. J. L.; Han, D.; Weng, Z.; He, G.; Parkin, I. P. Alleviation of Dendrite Formation on Zinc Anodes via Electrolyte Additives. *ACS Energy Lett.* **2021**, *6*, 395−403.

(15) Xu, Y.; Zhu, J.; Feng, J.; Wang, Y.; Wu, X.; Ma, P.; Zhang, X.; Wang, G.; Yan, X. A rechargeable aqueous zinc/sodium manganese oxides battery with robust performance enabled by Na_2SO_4 electrolyte additive. *Energy Storage Materials* **2021**, *38*, 299−308.

(16) Naveed, A.; Yang, H.; Yang, J.; Nuli, Y.; Wang, J. Highly reversible and rechargeable safe Zn batteries based on a triethyl phosphate electrolyte. *Angew. Chem., Int. Ed.* **2019**, *58*, 2760−2764.

(17) Xu, W.; Zhao, K.; Huo, W.; Wang, Y.; Yao, G.; Gu, X.; Cheng, H.; Mai, L.; Hu, C.; Wang, X. Diethyl ether as self-healing electrolyte additive enabled long-life rechargeable aqueous zinc ion batteries. *Nano Energy* **2019**, *62*, 275−281.

(18) Chang, N.; Li, T.; Li, R.; Wang, S.; Yin, Y.; Zhang, H.; Li, X. An aqueous hybrid electrolyte for low-temperature zinc-based energy storage devices. *Energy Environ. Sci.* **2020**, *13*, 3527−3535.

(19) Cao, L.; Li, D.; Hu, E.; Xu, J.; Deng, T.; Ma, L.; Wang, Y.; Yang, X.; Wang, C. Solvation structure design for aqueous Zn metal batteries. *J. Am. Chem. Soc.* **2020**, *142*, 21404−21409.

(20) Hou, Z.; Tan, H.; Gao, Y.; Li, M.; Lu, Z.; Zhang, B. Tailoring desolvation kinetics enables stable zinc metal anodes. *J. Mater. Chem. A* **2020**, *8*, 19367−19374.

(21) Gutmann, V. Empirical parameters for donor and acceptor properties of solvents. *Electrochim. Acta* **1976**, *21*, 661−670.

(22) Covington, A. K., Dickinson, T. Introduction and solvent properties. *Physical Chemistry of Organic Solvent Systems;* Plenum: New York, 1973, pp 1−22.

(23) Li, M.; Li, Z.; Wang, X.; Meng, J.; Liu, X.; Wu, B.; Han, C.; Mai, L. Comprehensive Understandings into Roles of Water Molecules in Aqueous Zn-Ion Batteries: From Electrolytes to Electrode Materials. *Energy Environ. Sci.* **2021**, *14*, 3796−3839.

(24) Schutt, T. C.; Hegde, G. A.; Bharadwaj, V. S.; Johns, A. J.; Maupin, C. M. Impact of water-dilution on the solvation properties of the ionic liquid 1-methyltriethoxy-3-ethylimidazolium acetate for model biomass molecules. *J. Phys. Chem. B* **2017**, *121*, 843−853.

(25) Yang, B.; Lang, H.; Liu, Z.; Wang, S.; Men, Z.; Sun, C. Three stages of hydrogen bonding network in DMF-water binary solution. *J. Mol. Liq.* **2021**, *324*, 114996.

(26) Hao, J.; Yuan, L.; Ye, C.; Chao, D.; Davey, K.; Guo, Z.; Qiao, S.-Z. Boosting Zinc Electrode Reversibility in Aqueous Electrolytes by Using Low-Cost Antisolvents. *Angew. Chem.* **2021**, *133*, 7442−7451.

(27) Hao, J.; Long, J.; Li, B.; Li, X.; Zhang, S.; Yang, F.; Zeng, X.; Yang, Z.; Pang, W.; Guo, Z. Toward High-Performance Hybrid Zn-Based Batteries via Deeply Understanding Their Mechanism and Using Electrolyte Additive. *Adv. Funct. Mater.* **2019**, *29*, 1903605.

(28) Zhao, J.; Zhang, J.; Yang, W.; Chen, B.; Zhao, Z.; Qiu, H.; Dong, S.; Zhou, X.; Cui, G.; Chen, L. Water-in-deep eutectic solvent" electrolytes enable zinc metal anodes for rechargeable aqueous batteries. *Nano Energy* **2019**, *57*, 625−634.

(29) Chen, S.; Lan, R.; Humphreys, J.; Tao, S. Salt-concentrated acetate electrolytes for a high voltage aqueous Zn/MnO_2 battery. *Energy Storage Materials* **2020**, *28*, 205−315.

(30) Sun, P.; Ma, L.; Zhou, W.; Qiu, M.; Wang, Z.; Chao, D.; Mai, W. Simultaneous Regulation on Solvation Shell and Electrode Interface for Dendrite-Free Zn Ion Batteries: Achieved by a Low-Cost Glucose Additive. *Angew. Chem.* **2021**, *133*, 18395−18403.

(31) Zeng, X.; Mao, J.; Hao, J.; Liu, J.; Liu, S.; Wang, Z.; Wang, Y.; Zhang, S.; Zheng, T.; Liu, J.; Rao, P.; Guo, Z. Electrolyte Design for *In Situ* Construction of Highly Zn^{2+}-Conductive Solid Electrolyte Interphase to Enable High-Performance Aqueous Zn-Ion Batteries under Practical Conditions. *Adv. Mater.* **2021**, *33*, 2007416.

(32) Ma, L.; Pollard, T. P.; Zhang, Y.; Schroeder, M. A.; Ding, M. S.; Cresce, A. V.; Sun, R.; Baker, D. R.; Helms, B. A.; Maginn, E. J.; Wang, C.; Borodin, O.; Xu, K. Functionalized Phosphonium Cations Enable Zinc Metal Reversibility in Aqueous Electrolytes. *Angew. Chem., Int. Ed.* **2021**, *60*, 12438−12445.

(33) Li, D.; Cao, L.; Deng, T.; Liu, S.; Wang, C. Design of a Solid Electrolyte Interphase for Aqueous Zn Batteries. *Angew.Chem. Int.Ed.* **2021**, *60*, 13035−13041.

(34) Dong, Y.; Miao, L.; Ma, G.; Di, S.; Wang, Y.; Wang, L.; Xu, J.; Zhang, N. Non-concentrated aqueous electrolytes with organic solvent additives for stable zinc batteries. *Chem. Sci.* **2021**, *12*, 5843−5852.
(35) Verma, V.; Chan, R. M.; Jia Yang, L.; Kumar, S.; Sattayaporn, S.; Chua, R.; Cai, Y.; Kidkhunthod, P.; Manalastas, W.; Srinivasan, M. Chelating Ligands as Electrolyte Solvent for Rechargeable Zinc-Ion Batteries. *Chem. Mater.* **2021**, *33*, 1330−1340.
(36) Chu, Y.; Zhang, S.; Wu, S.; Hu, Z.; Cui, G.; Luo, J. *In situ* built interphase with high interface energy and fast kinetics for high performance Zn metal anodes. *Energy Environ. Sci.* **2021**, *14*, 3609−3620.
(37) Zhang, Y.; Zhu, M.; Wu, K.; Yu, F.; Wang, G.; Xu, G.; Wu, M.; Liu, H.; Dou, S.; Wu, C. An in-depth insight of a highly reversible and dendrite-free Zn metal anode in an hybrid electrolyte. *J. Mater. Chem. A* **2021**, *9*, 4253−4261.
(38) Wu, H.; Gu, X.; Huang, P.; Sun, C.; Hu, H.; Zhong, Y.; Lai, C. Polyoxometalate driven dendrite-free zinc electrodes with synergistic effects of cation and anion cluster regulation. *J. Mater. Chem. A* **2021**, *9*, 7025−7033.
(39) Qin, R.; Wang, Y.; Zhang, M.; Wang, Y.; Ding, S.; Song, A.; Yi, H.; Yang, L.; Song, Y.; Cui, Y.; Liu, J.; Wang, Z.; Li, S.; Zhao, Q.; Pan, F. Tuning Zn^{2+} coordination environment to suppress dendrite formation for high-performance Zn-ion batteries. *Nano Energy* **2021**, *80*, 105478.
(40) Sun, C.; Wu, C.; Gu, X.; Wang, C.; Wang, Q. Interface Engineering via $Ti_3C_2T_x$ MXene Electrolyte Additive toward Dendrite-Free Zinc Deposition. *Nano-Micro Lett.* **2021**, *13*, 89.
(41) Cao, L.; Li, D.; Pollard, T.; Deng, T.; Zhang, B.; Yang, C.; Chen, L.; Vatamanu, J.; Hu, E.; Hourwitz, M. J.; Ma, L.; Ding, M.; Li, Q.; Hou, S.; Gaskell, K.; Fourkas, J. T.; Yang, X.-Q.; Xu, K.; Borodin, O.; Wang, C. Fluorinated interphase enables reversible aqueous zinc battery chemistries. *Nat. Nanotechnol.* **2021**, *16*, 902−910.
(42) Wang, S.; Wang, Z.; Yin, Y.; Li, T.; Chang, N.; Fan, F.; Zhang, H.; Li, X. A highly reversible zinc deposition for flow batteries regulated by critical concentration induced nucleation. *Energy Environ. Sci.* **2021**, *14*, 4077−4084.
(43) Kundu, D.; Vajargah, S. H.; Wan, L.; Adams, B.; Prendergast, D.; Nazar, L. F. Aqueous vs. nonaqueous Zn-ion batteries: consequences of the desolvation penalty at the interface. *Energy Environ. Sci.* **2018**, *11*, 881−892.
(44) Zhao, Z.; Zhao, J.; Hu, Z.; Li, J.; Li, J.; Zhang, Y.; Wang, C.; Cui, G. Long-life and deeply rechargeable aqueous Zn anodes enabled by a multifunctional brightener-inspired interphase. *Energy Environ. Sci.* **2019**, *12*, 1938−1949.
(45) Hao, J.; Li, B.; Li, X.; Zeng, X.; Zhang, S.; Yang, F.; Liu, S.; Li, D.; Wu, C.; Guo, Z. An In-Depth Study of Zn Metal Surface Chemistry for Advanced Aqueous Zn-Ion Batteries. *Adv. Mater.* **2020**, *32*, 2003021.
(46) Loerting, T.; Bernard, J. Aqueous carbonic acid (H_2CO_3). *ChemPhysChem* **2010**, *11*, 2305.
(47) *Recommended Methods for Purification of Solvents and Tests for Impurities*; Coetzee, J. F., Ed.; Pergamon Press: Oxford, 1982; pp 32−37.
(48) Li, C.; Shyamsunder, A.; Hoane, A. G.; Long, D. M.; Kwok, C. Y.; Kotula, P. G.; Zavadil, K. R.; Gewirth, A. A.; Nazar, L. F. Highly reversible Zn anode with a practical areal capacity enabled by a sustainable electrolyte and superacid interfacial chemistry. *Joule* **2022**, *6*, 1103−1120.
(49) Chowdhury, F. A.; Yamada, H.; Higashii, T.; Goto, K.; Onoda, M. CO_2 Capture by Tertiary Amine Absorbents: A Performance Comparison Study. *Ind. Eng. Chem. Res.* **2013**, *52*, 8323−8331.
(50) Winiarski, J.; Tylus, W.; Winiarska, K.; Szczygieł, I.; Szczygieł, B. XPS and FT-IR characterization of selected synthetic corrosion products of zinc expected in neutral environment containing chloride ions. *J. Spectrosc.* **2018**, *2018*, 2079278.
(51) Qiu, H.; Hu, R.; Du, X.; Chen, Z.; Zhao, J.; Lu, G.; Jiang, M.; Kong, Q.; Yan, Y.; Du, J.; Zhou, X.; Cui, G. Eutectic Crystallization Activates Solid-State Zinc-Ion Conduction. *Angew. Chem., Int. Ed.* **2022**, *61*, No. e202113086.
(52) Duer, M. J. *Solid State NMR Spectroscopy: Principles and Applications*; Blackwell Science, Oxford, UK, 2018; pp 239−279.
(53) He, X.; Zhu, Y.; Epstein, A.; Mo, Y. Statistical variances of diffusional properties from ab initio molecular dynamics simulations. *npj Comput. Mater.* **2018**, *4*, 18.
(54) Ikeda, S.; Kanbayashi, Y.; Normua, K.; Kasai, A.; Ito, K. Solid electrolytes with multivalent cation conduction (2) zinc ion conduction in $ZnZrPO_4$ system. *Solid State Ionics* **1990**, *40*−*41*, 79−82.
(55) Canepa, P.; Bo, S.-H.; Gautam, G. S.; Key, B.; Richards, W. D.; Shi, T.; Tian, Y.; Wang, Y.; Li, J.; Ceder, G. High magnesium mobility in ternary spinel chalcogenides. *Nat. Commun.* **2017**, *8*, 1759.
(56) Martinolich, A. J.; Lee, C.-W.; Lu, I-T.; Bevilacqua, S. C.; Preefer, M. B.; Bernardi, M.; Schleife, A.; See, K. A. Solid-State Divalent Ion Conduction in $ZnPS_3$. *Chem. Mater.* **2019**, *31*, 3652−3661.
(57) Shi, S.; Qi, Y.; Li, H.; Hector, L. G. Defect Thermodynamics and Diffusion Mechanisms in Li_2CO_3 and Implications for the Solid Electrolyte Interphase in Li-Ion Batteries. *J. Phys. Chem. C* **2013**, *117*, 8579−8593.
(58) Pan, J.; Cheng, Y.-T.; Qi, Y. General method to predict voltage-dependent ionic conduction in a solid electrolyte coating on electrodes. *Phys. Rev. B* **2015**, *91*, 134116.
(59) Ramasubramanian, A.; Yurkiv, V.; Foroozan, T.; Ragone, M.; Shahbazian-Yassar, R.; Mashayek, F. Lithium Diffusion Mechanism through Solid−Electrolyte Interphase in Rechargeable Lithium Batteries. *J. Phys. Chem. C* **2019**, *123*, 10237−10245.
(60) Feng, M.; Pan, J.; Qi, Y. Impact of Electronic Properties of Grain Boundaries on the Solid Electrolyte Interphases (SEIs) in Li-ion Batteries. *J. Phys. Chem. C* **2021**, *125*, 15821−15829.
(61) Zhao, C. X.; Liu, J.-N.; Yao, N.; Wang, J.; Ren, D.; Chen, X.; Li, B. Q.; Zhang, Q. Can Aqueous Zinc−Air Batteries Work at Sub-Zero Temperatures? *Angew. Chem., Int. Ed.* **2021**, *133*, 15409−15413.
(62) Zhang, N.; Cheng, F.; Liu, J.; Wang, L.; Long, X.; Liu, X.; Li, F.; Chen, J. Rechargeable aqueous zinc-manganese dioxide batteries with high energy and power densities. *Nat. Commun.* **2017**, *8*, 405.
(63) Zhang, T.; Tang, Y.; Guo, S.; Cao, X.; Pan, A.; Fang, G.; Zhou, J.; Liang, S. Fundamentals and perspectives in developing zinc-ion battery electrolytes: a comprehensive review. *Energy Environ. Sci.* **2020**, *13*, 4625−4665.

https://doi.org/10.1021/acsenergylett.3c00154
ACS Energy Lett. 2023, 8, 1613−1625